Creep deformation and mechanisms in Haynes 230 at 800 °C and 900 °C

Garrett J. Pataky [a,*], Huseyin Sehitoglu [a,1], Hans J. Maier [b]

[a] Department of Mechanical Science and Engineering, University of Illinois at Urbana-Champaign, 1206 W. Green St., Urbana, IL 61801, USA
[b] Institut für Werkstoffkunde (Materials Science), Leibniz Universität Hannover, An der Universität 2, D-30823 Garbsen, Germany

ARTICLE INFO

ABSTRACT

Creep was studied in Haynes 230, a material candidate for the very high temperature reactor's intermediate heat exchanger, at 800 °C and 900 °C. This study focused on the differences between the behavior at the two elevated temperature, and using the microstructure, grain boundary serrations and triple junction strain concentrations were quantitatively identified. There was significant damage in the 900 °C samples and the creep was almost entirely tertiary. In contrast, the 800 °C sample exhibited secondary creep. Using an Arrhenius equation, the minimum creep rate exponents were found to be $n \approx 3$ and $n \approx 5$ for 900 °C and 800 °C, respectively. The creep mechanisms were identified as solute drag for $n \approx 3$ and dislocation climb for $n \approx 5$. Strain concentrations were identified at triple junctions and grain boundary serrations using high resolution digital image correlation overlaid on the microstructure. The grain boundary serrations restrict grain boundary sliding which may reduce the creep damage at triple junctions and extend the creep life of Haynes 230 at elevated temperatures.

© 2013 Elsevier B.V. All rights reserved.

1. Introduction

The very high temperature reactors (VHTR) currently being developed will boost their economic efficiency over current reactors by elevating operating temperatures. This will allow for both the production of electricity and helium [1]. The intermediate heat exchangers in the system must be able to operate at temperatures of 900 °C, putting a huge demand on the materials employed. One of the proposed materials is Haynes 230, developed by Haynes International, Inc. A great amount of knowledge is still needed to understand how Haynes 230 creeps before it can be implemented to operate at these high temperatures. Of particular interest is the deterioration of properties between 800 °C and 900 °C.

Voids were first identified in crept materials over a half century ago [2,3]. Further studies by Greenwood found these cavities, based on the sliding of the grain boundaries, led to the failure of the material [4,5]. Using a comprehensive collection of data, isothermal fracture maps separating intergranular and transgranular fracture based on temperature and loading were constructed [6]. These maps were also able to indicate what creep mechanism was most likely to be dominant. In the present study, the creep damage created voids, which subsequently led to large localized deformation in the material, and thus the material exhibited mostly intergranular failure, as predicted due to the temperatures and stresses the samples were subjected to.

Two main areas of focus for failure along grain boundaries are triple junctions and precipitates. Both of these can lead to stress concentrations caused by grain boundary sliding during creep conditions [7]. Argon, Chen, and Lau modeled these two forms of grain boundary decohesion which had been previously experimentally observed [8]. Precipitates on the grain boundaries restrict the sliding of the grain boundaries during transient loading, while triple junctions tend to dominate as stress concentrations once the load supported by these precipitates reaches a critical limit. Using stress functions and power-law creep, singularities around the triple junctions and precipitates were modeled [9]. This was also implemented in a finite element model study [10]. The presence of carbides in nickel-based superalloys, in particular Haynes 230, on grain boundaries can cause serrations of grain boundaries [11], acting as particles restricting grain boundary sliding.

Haynes 230 has been the focus of many studies and its deformation behavior is still being characterized. Since the material will be used at elevated temperatures, oxidation rates were studied and Haynes 230 was found to have a high oxidation resistance [12,13]. Fatigue crack growth behavior has been studied at room temperature and elevated temperatures, showing a decrease in the crack growth resistance as temperature rises [14–16]. The creep-fatigue behavior was recently discussed by Chen et al. and Haynes 230 exhibited greater fatigue-creep life than Alloy 617 [17]. At increased hold times during the creep-fatigue cycle, the life was observed to decrease in Haynes 230. The creep behavior was recently investigated and compared to that of Haynes 282 up to 815 °C [18]. Haynes 282 showed significantly greater creep resistance than Haynes 230.

---

* Corresponding author. Tel.: +1 217 333 3859.
  E-mail addresses: pataky2@illinois.edu (G.J. Pataky), huseyin@illinois.edu (H. Sehitoglu), maier@iw.uni-hannover.de (H.J. Maier).
[1] Tel.: +1 217 333 4112.

The current study advances our understanding of the creep behavior that Haynes 230 exhibits by comparing experimental results at 800 °C and 900 °C. The minimum creep rates were used to contrast the two temperatures in terms of deformation mechanisms. To better understand how the microstructure deforms, high resolution digital image correlation, along with optical images of the microstructure, was utilized to identify the areas of the microstructure prone to developing strain concentrations during deformation. Other studies have shown that grain boundary serrations lead to a lower creep rate in nickel-based superalloys [19,20]. The present study has found a concentration of strain at these serrations, which may impede grain boundary sliding. Strain concentrations were also identified at triple junctions. The current study quantifies these strain concentrations and discusses the large difference in the creep behavior between 800 °C and 900 °C.

2. Materials and experimental procedure

2.1. Materials

This study used commercially available Haynes 230. Haynes 230 is a solid-solution strengthened alloy, and the additions of chromium, tungsten, and molybdenum contribute to the high temperature properties. The chemical composition of the sheet is provided in Table 1. A wide range of grain sizes, 30–250 μm, were observed in the microstructure, with the grains being equiaxed. The received sheet was 2.38 mm (3/32″) thick. Sheet thick "dog-bone" specimens with a gauge length of 25.00 mm and a width of 4.00 mm were electrical discharge machined (EDM). A schematic of the specimen geometry is given in Fig. 1.

2.2. Experimental procedure

Since digital image correlation (DIC) was used to capture the displacements of the deformed specimens, the specimen surfaces had to be prepared with a speckle pattern. Two separate procedures were used since this study included both in situ and ex situ experiments. For the in situ samples, due to the glowing of the material at 800 °C and 900 °C, a thin layer of white paint was applied prior to the application of the speckle pattern. Before applying the white paint, each sample was mechanically polished with grit paper up to P2400 to create a flat surface, and then they were subsequently roughened with P320 paper to help the white paint adhere to the surface. The white paint used was VHT Flame-Proof flat white ceramic coating (SP101) with a temperature rating up to 1093 °C. This prevented the images from being oversaturated and prevented the speckle pattern from being changed by oxidation. The white paint required a three-step curing process as indicated by the manufacturer, but the curing temperature did not exceed 315 °C. On top of the white paint, black paint was airbrushed creating the random pattern for DIC. The black paint was VHT FlameProof flat black ceramic coating (SP102).

For the ex situ, high resolution DIC samples, the surface was mechanically polished to a mirror finish using abrasive paper and a final step of 0.3 μm silica powder. The sample was then heated in an oven at 900 °C for 7 min and water quenched. The small layer of oxidation that formed allowed for the grain boundaries to be
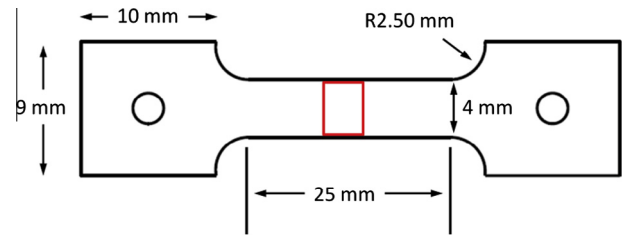

Fig. 1. Schematic of the dog-bone specimen geometry. The red box represents the area imaged during testing. (For interpretation of the references to colour in this figure legend, the reader is referred to the web version of this article.)

visible under an optical microscope. An area was marked off, and optical images were taken using the microscope at a magnification of 10× to provide insight into the microstructure. The sample was then prepared using the in situ procedure. Another set of optical images at 10× were captured as the reference images for DIC. This type of sample will be referred to as the ex situ sample.

A servo-hydraulic load frame with a 7.5 kN load cell was used during the experiments and the specimens were heated using induction heating. A type-K thermocouple was welded in the middle of the back of the gauge section. All experiments were performed in air. The temperature of the specimens was raised from room temperature to either 800 °C or 900 °C at a rate of 75 °C per minute. The temperate was kept within a tolerance of ±3 °C for the duration of the tests using a temperature controller connected to the induction heater. The specimen surface was illuminated using white light. An IMI 202FT digital camera was used to record the images during the experiments, capturing an image every 30 s. The camera resolution was 1600 pixels × 1200 pixels and a field of view of 4.00 mm by 3.00 mm was imaged for the in situ experiments. For the in situ tests, images were captured throughout the entire experiment until failure or the test was suspended. A photograph of the experimental setup is shown in Fig. 2. The ex situ tests were halted after a predetermined time in order to capture images using the optical microscope. These images were captured in the same area as the pre-test images. The entire visible area of the deformed images was correlated back to the original, undeformed reference images using a commercially available image correlation program. The horizontal and vertical displacements were differentiated using a small strain assumption in order to find the strain fields. The average measure of noise in the strain was 5×10^{-4} with a maximum local nose value of 0.002. For more
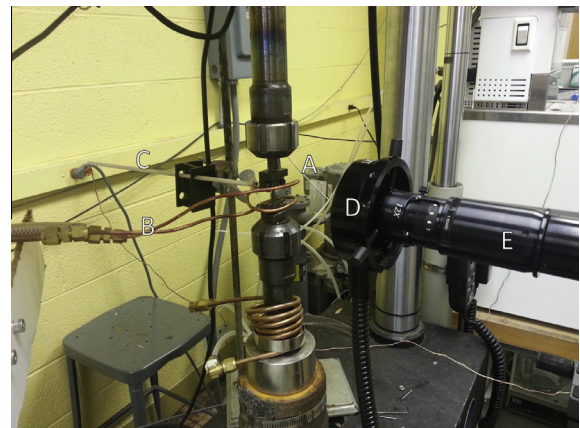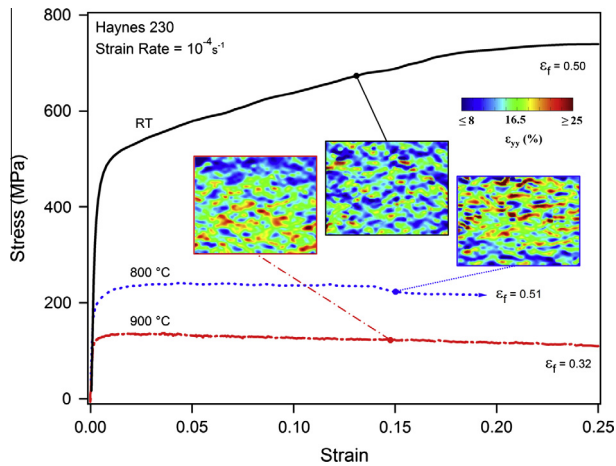
Table 1
Chemical composition (wt%) of Haynes 230 studied.

Al	B	C	Co	Cr	Cu	Fe	La	Mn
0.35	0.005	0.1	0.16	22.14	0.04	1.14	0.015	0.5
Mo	Ni	P	S	Si	Ti	W	Zr	
1.25	Bal	0.005	0.002	0.49	0.01	14.25	0.01	

Fig. 2. An example of the experimental setup. (A) Specimen in the load frame, (B) Induction coils, (C) Type-K thermocouple, (D) Illumination and (E) Lens and Camera.

Fig. 3. Stress–strain data for Haynes 230 at room temperature (RT), 800 °C, and 900 °C. DIC strain fields at approximately 15% strain show localization in the two high temperature cases in contrast to the homogeneous field at RT.

information about the DIC technique, see Refs. [21,22]. For more information on the high resolution ex situ DIC, see Ref. [23].

For transmission electron microscopy (TEM) 1 mm thick disks were sectioned with a low-speed diamond saw parallel to the loading axis from the failed specimens, and then mechanically ground and polished down to 0.15 mm foil thickness. Large electron transparent areas were obtained in these foils by conventional twin jet polishing using a solution consisting of 5% perchloric acid in ethanol at −20 °C and 15 V. The TEM was operated at a nominal voltage of 200 kV and a double-tilt specimen holder was employed for imaging under two-beam conditions.

3. Results

3.1. Tensile tests

Uniaxial tension tests were performed at a strain rate of $10^{-4} \, s^{-1}$ on Haynes 230 at three temperatures: room temperature, 800 °C, and 900 °C. These tests were performed to determine the baseline data for the mechanical properties. As expected, the yield

stress decreased with increasing temperature. Using a 0.2% offset, the yield stresses were found to be 415 MPa at room temperature, 197 MPa at 800 °C, and 123 MPa at 900 °C. These results are shown in Fig. 3. There are distinct differences between the two high temperature samples and the room temperature sample; the room temperature sample exhibits hardening throughout the test while both high temperature cases show slight softening behavior, which is more distinct in the 900 °C experiment.

The specimens fractured at 50% strain at room temperature, 51% at 800 °C, and 32% at 900 °C. There is a significant difference in the fracture strains for the two high temperature results. A possible explanation for this is the large voids and necking, visible to the eye, present in the 900 °C sample. In contrast, the 800 °C sample only exhibited necking. The difference in damage behavior during the tensile tests was a precursor for what was observed in the creep tests.

3.2. Creep results

The creep tests were conducted at relatively high stresses for the temperatures considered in order to produce creep strains in a reasonable time period. The results of these creep tests are presented in Fig. 4. The strains in this figure are the averaged DIC axial strains found in the area imaged during the experiments. There is a noticeable difference in behavior between the two high temperatures. In the 900 °C experiments (Fig. 4a), the secondary creep lasts for a few minutes in each of the tests. Almost the entire creep curve consists of tertiary creep. Surface damage and voids were visible early on in the experiments, consistent with the damage expected. Contrary to these results, the 800 °C experiments (Fig. 4b) had prolonged periods of secondary creep. The tests performed at loads of 50 and 75 MPa were halted before the samples failed. The visible surface damage that was present in the 900 °C experiments was not present in the 800 °C experiments.

Further information concerning the strains developed during creep was found using high resolution ex situ DIC. Two samples of Haynes 230 were crept at 900 °C with a stress of 50 MPa for 2 h and 10 h each. After the test was suspended, the material was unloaded and cooled to room temperature leaving residual plastic strains to be measured with DIC. The average strain was 0.26% for the 2 h sample and 0.88% for the 10 h sample. The two
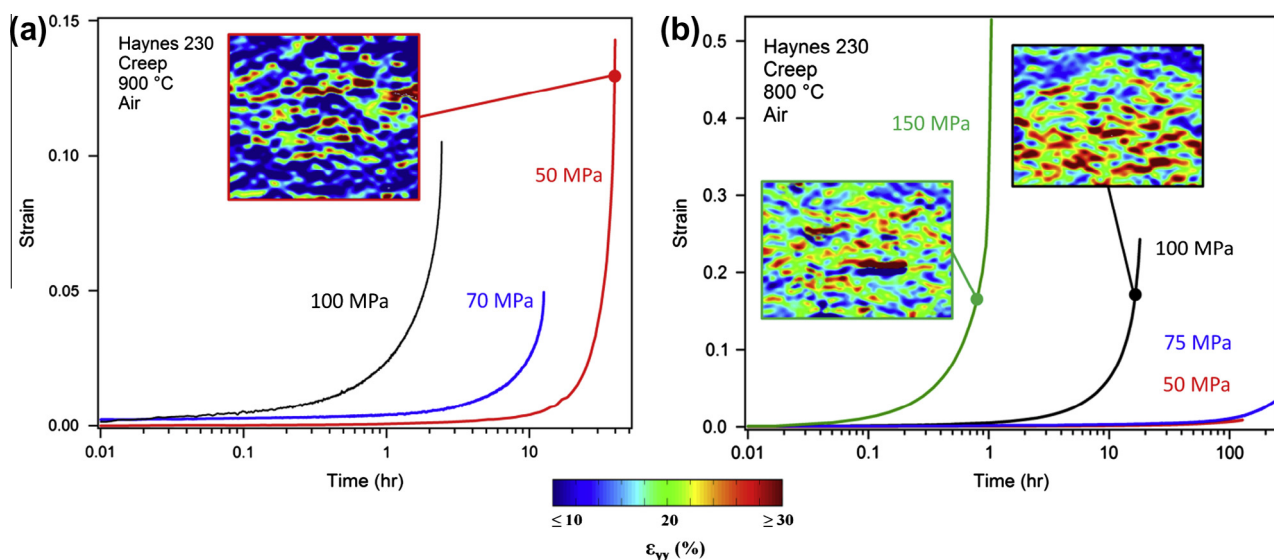
Fig. 4. Strain versus time data for creep tests of Haynes 230 at 800 °C and 900 °C at several load levels. Steady state creep is more readily observed in the 800 °C samples while both tests show localized strains greater than 30%.
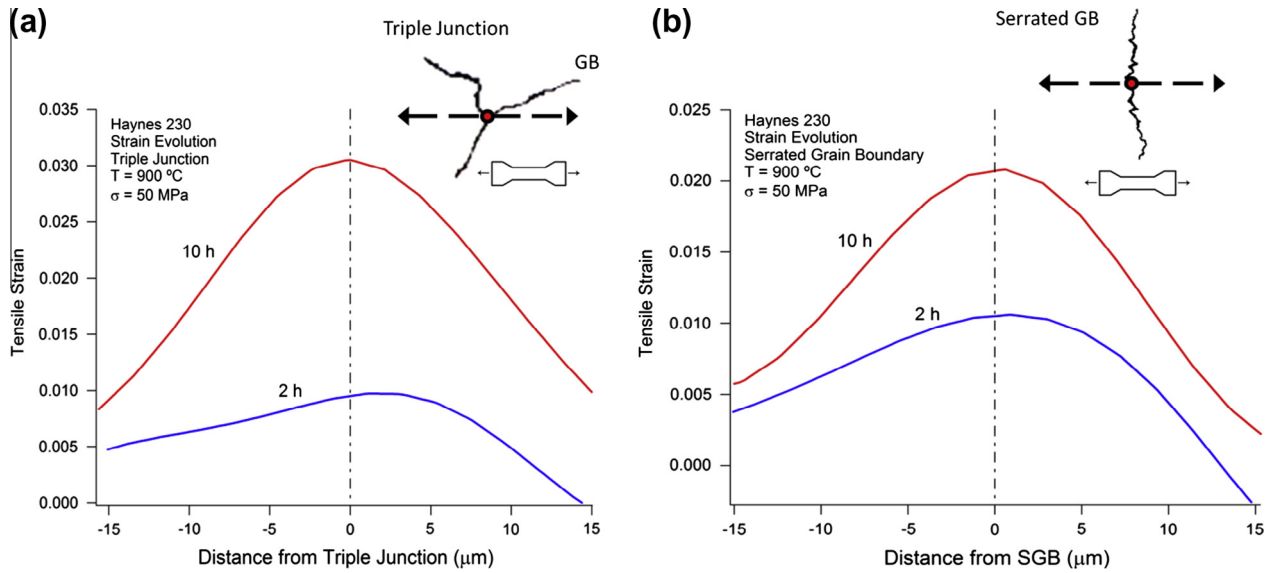
Fig. 5. Strain magnitudes as a function of distance found at serrated grain boundaries and triple junctions. The red dot in the schematics shows the 0 μm measurement point for (a) triple junction and (b) to serrated grain boundaries. (For interpretation of the references to color in this figure legend, the reader is referred to the web version of this article.)
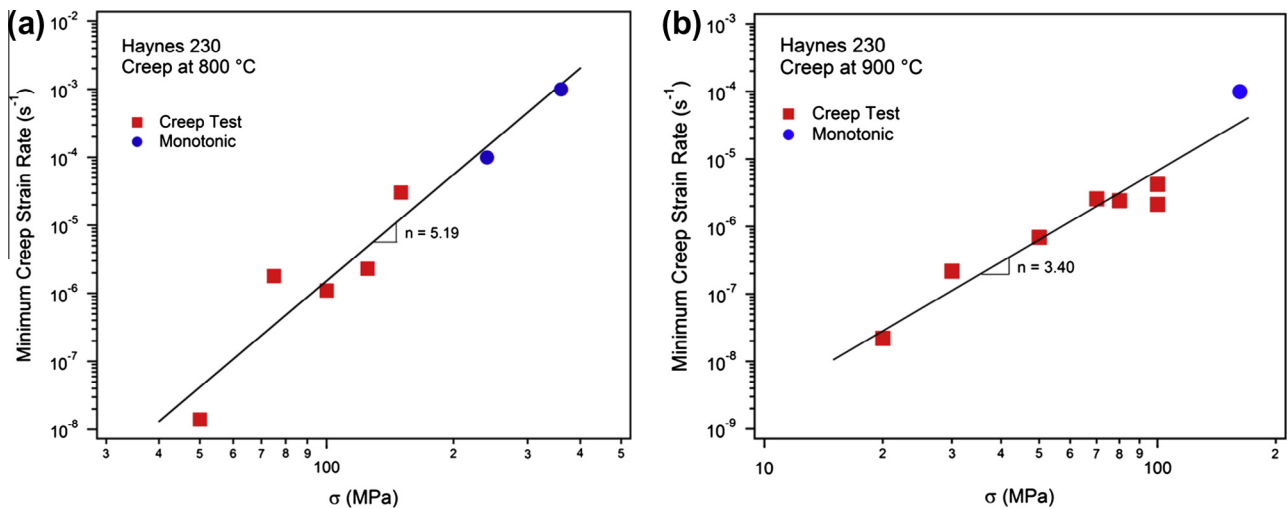
Fig. 6. The minimum creep rate plotted as a function of the stress applied loading for creep of Haynes 230. The creep at 800 °C corresponds to a creep exponent of $n \approx 5$ (dislocation climb mechanism) and the 900 °C results produce a creep exponent of $n \approx 3$ (solute drag mechanism).

Table 2
Creep constants summary of Haynes 230 [s^{-1}].

| Temp. (°C)	Creep coefficient (A)	Creep exponent (n)
800	6.38E-17	5.19
900	1.89E-09	3.40

main areas of strain concentration were focused around serrated grain boundaries and triple junctions. The sample suspended at 2 h showed less strain concentration than the 10 h sample, consistent with the increasing average strain. DIC was used to quantitatively obtain the trend of strain distribution at these two points, and showed a peak at the serrated grain boundary and triple junction, as indicated in Fig. 5. The strains measured were tensile strains aligned with the loading direction and were found to be orders of magnitude higher than the average strain of the area. These results showed that there was a trend of increasing strain concentration at magnitudes much higher than the average strain

as time progresses, with the peak remaining at the serrated grain boundary or triple junction. Further discussion of this will be given in Section 4.1.

The minimum secondary creep rates, $\dot{\varepsilon}_{ss,min}$, were assumed to follow the fundamental Arrhenius equation:

$$\dot{\varepsilon}_{ss,min} = A(\sigma)^n \tag{1}$$

where A is the creep constant, σ is the nominal stress, and n is the creep exponent. In order to better distinguish which mechanisms of creep was active, the minimum strain rates for each experiment were plotted against the nominal stress the sample was loaded at in Fig. 6. The constants fitted are given in Table 2. Consistent with the creep results, the strain rates also show a difference in behavior between the two high temperatures. At 900 °C, the creep exponent was found to be $n = 3.4$. This can be approximated to $n = 3$ where the rate limiting mechanism is dislocation glide, also known as solute drag [24]. At 800 °C, the creep exponent was found to be $n = 5.17$, which is representative of dislocation climb ($n = 5$) being
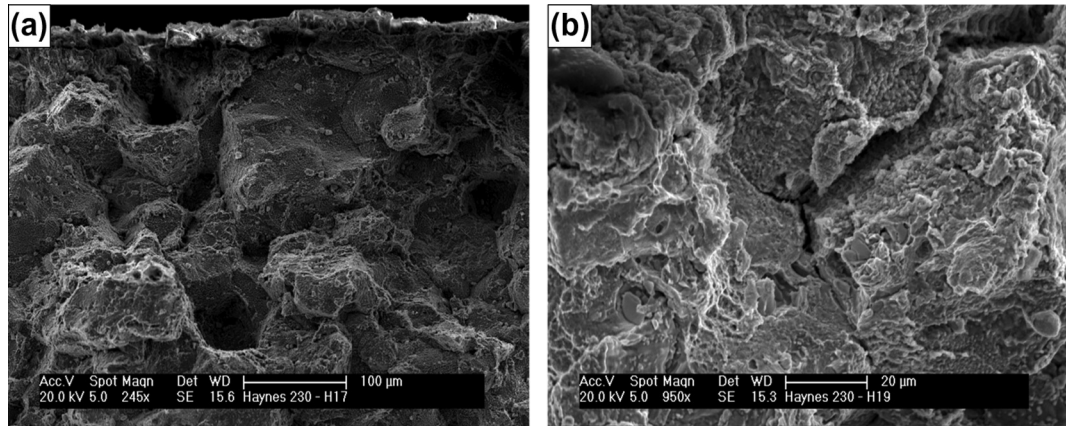
Fig. 7. SEM micrographs of the fracture surface from samples crept at 900 °C. (a) Intergranular cracking and voids are evident. (b) A cracked triple junction on the fracture surface.
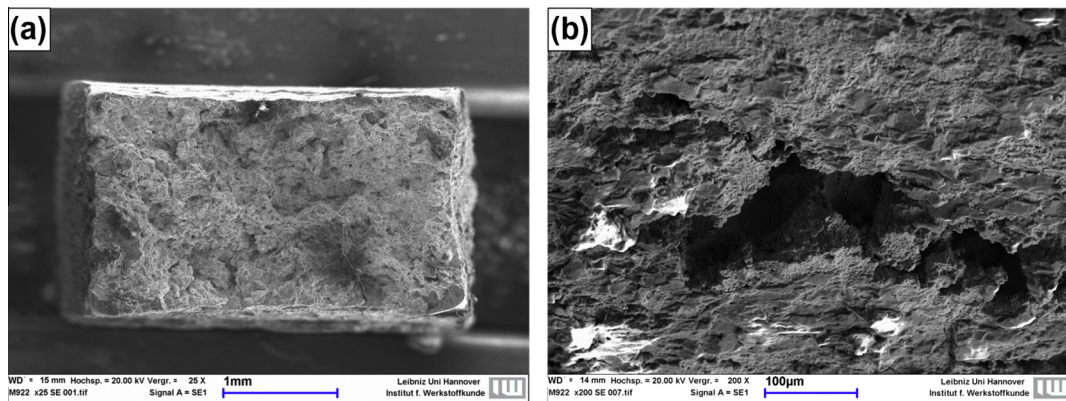
Fig. 8. SEM micrographs of the fracture surface and a secondary crack from a sample crept at 800 °C. (a) The fracture surface of the sample showing high levels of ductility and a mixture of intergranular and transgranular cracking. (b) A secondary crack below the failed section showing intergranular cracking.
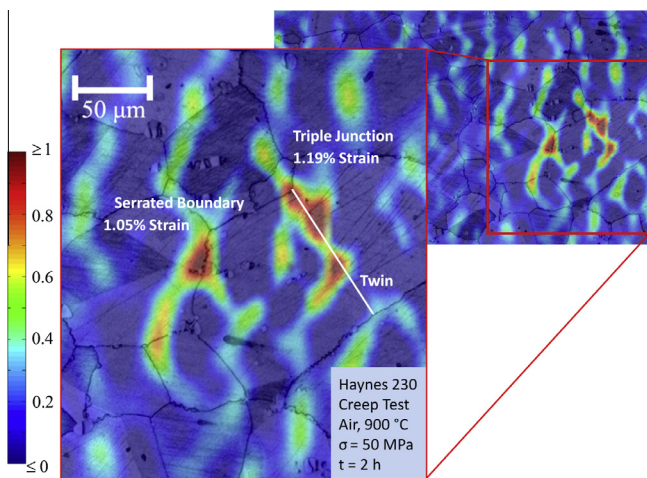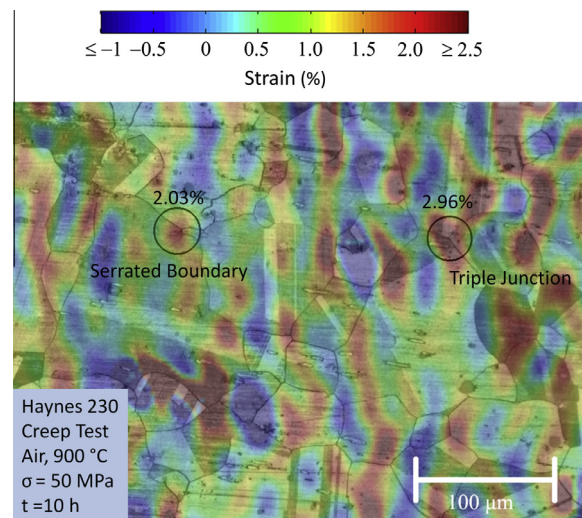

Fig. 9. DIC axial strain field (average strain of 0.26%) after 2 h of creep at 900 °C with a load of 50 MPa overlaid on an optical micrograph of the microstructure at a magnification of 10×. Two areas of localized strain were observed: on a serrated grain boundary and at the triple junction of a twin and two grain boundaries.

Fig. 10. DIC axial strain field (average strain of 0.88%) after 10 h of creep at 900 °C with a load of 50 MPa overlaid on an optical micrograph of the microstructure at 10×. High levels of localized strain were found at a triple junction and a serrated grain boundary.

the rate limiting creep mechanism [25]. More discussion of this result will be presented in Section 4.1.

3.3. SEM of crept material

After the samples of Haynes 230 had been crept, scanning electron microscopy (SEM) was performed to analyze the fracture

surfaces. First analyzing the micrographs in Fig. 7 from samples experimented at 900 °C, it is evident that the samples show intergranular failure. In Fig. 7a, despite the oxidation, the cracking can be observed along the grain boundaries and several large voids are depicted. In Fig. 7b, cracking at a triple junction is apparent.
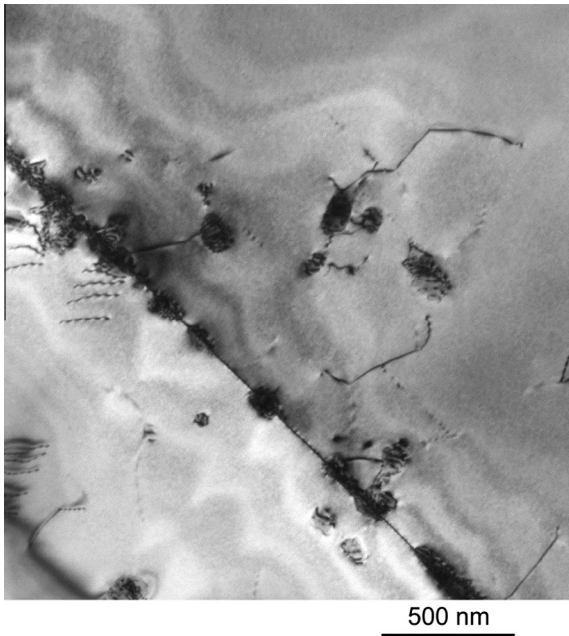
Fig. 11. A TEM micrograph from a sample crept at 900 °C at a stress of 100 MPa showing dislocation-carbide interactions with carbides present in the boundary. The carbides in the grain boundary are the cause of serrated grain boundaries.

Cracking along grain boundaries is also visible in the upper right portion of the micrograph. This result was to be expected due to the temperature and stresses the sample was subjected to.

The samples crept at 800 °C showed mainly intergranular fracture, but there was also evidence of transgranular failure along the fracture surface, shown in Fig. 8a. Fig. 8b depicts a secondary, intergranular crack that formed below the area of failure. This sample had much more ductility than the 900 °C sample, which could contribute to the longer observed creep life. There was also less damage, explicitly a lack of large voids, found along the fracture plane in this specimen.

4. Discussion

4.1. Grain boundary serrations and triple junctions

The strain heterogeneity at the microscale was investigated for areas of strain concentrations. This was performed using high resolution digital image correlation and observing the strain fields overlaid on the microstructure. The advantage of DIC is that as the magnification is increased, the spatial resolution improves allowing for strain measurements on the microscale [21,23].

As indicated in the Introduction, precipitates in the grain boundaries and triple junctions are known to be sources of failure during creeping conditions. In Haynes 230, these are M_6C and $M_{23}C_6$ carbides. In order to investigate these as potential points of failure, high resolution DIC had to be performed on the sample using the ex situ procedure described in Section 2.2 and preliminary results given in Section 3.2. The samples of interest were used in a creep test performed at 900 °C with a nominal stress of 50 MPa and were arrested after 2 h and 10 h. DIC was performed and the strain fields were overlaid on the microstructure and strain concentrations were investigated. The axial strains were investigated as shear strain concentration was present in the same locations, but with lower magnitude.

The resulting axial strain fields are presented for 2 h and 10 h in Figs. 9 and 10, respectively. Both figures show strain concentrations on serrated grain boundaries and at triple junctions. This result is consistent with the review presented by Argon [7]. As the grain boundaries slide during creep, the pinning of the serrated grain boundaries by carbides leads to an increase in the stress fields. The triple junctions act as sites of void formation, and if allowed to creep further, the voids would grow and merge with cavitations on the grain boundaries leading to cracks. These are competing processes since the grain boundaries are restricted from sliding by the carbides delaying damage, while the triple junctions indicate the formation of voids.

Further discussion of the grain boundaries serrations (GBS) is needed. In a previous study, the serrations in Haynes 230 were found to be caused by $M_{23}C_6$ carbides, where M is mostly chromium [11]. M_6C carbides, with M being mostly tungsten, are also present in Haynes 230, but at solutionizing temperatures, these carbides dissolve introducing a supersaturation of C into the matrix. The supersaturation of C can lead to further nucleation and growth of the $M_{23}C_6$ carbides [11]. Literature concerning GBS has found that they can lower the creep rate and reduce crack propagation since grain boundary sliding is restricted [19,20]. This is experimentally observed in the crept Haynes 230 sample as the strains present on the GBS may be due to this restriction of sliding. TEM supporting the presence of carbides at the boundaries is shown in Fig. 11. This micrograph depicts dislocation-carbide interactions while the carbides are pinned in the (sub)grain boundary from a specimen crept at 100 MPa until failure after an hour. Future studies of Haynes 230 are needed to observe how these strains develop during the life of a creeping sample. A heat treatment encouraging the creation of GBS for Haynes 230 by increasing the nucleation and growth of granular $M_{23}C_6$ carbides [11] may lead to decreased creep rates, especially at 900 °C, which could lead to prolong the secondary creep life and expand the use of this superalloy.

4.2. Creep exponents

As previously indicated in Section 3.2, Haynes 230 exhibits different mechanisms limiting the creep rate at the different elevated temperatures. Weertman was the first to describe the dislocation activities that led to these two creep mechanisms [24,25]. Much work has been performed since his discovery in order to describe the differences between the solute drag mechanism and the dislocation climb mechanism. A brief explanation of the two mechanisms is presented below.

A creep exponent of $n \approx 3$, found for the 900 °C creep, is synonyms with solute drag during creep, as originally found by Cottrell and Jawson [26]. In this case, dislocations that are gliding are dragging solute atoms with them limiting the velocity of the gliding. The rate of glide is assumed proportional to the applied stress, and the stress a dislocation applies on its neighbor is inversely proportional to the dislocation density. The three power law proportionality of the creep rate to the applied stress is approximated by the product of the dislocation density, Burgers vector, and the rate of glide [27]. A review of the dragging processes responsible for this mechanism can be found in [28]. Of special note is the proposed dragging process which is due to the segregation of atoms at stacking faults [29]. In Haynes 230, the addition of tungsten lowers the stacking fault energy which could reduce the recovery rate and in consequence, reduce the creep rate [30].

For the creep rate to be proportional to the fifth power, $n \approx 5$, an additional σ^2 must be introduced. Recall that this is representative of the creep occurring at 800 °C. This behavior involves the formation of dislocation networks and sub-grains. As dislocation loops expand by glide and climb, they eventually annihilate, and the interaction of edge and screw dislocations forms dislocation networks. The resulting mixed dislocations in the networks, or subgrain networks, control the rate that vacancies are absorbed and emitted [31]. The diffusion coefficient for the vacancies is then
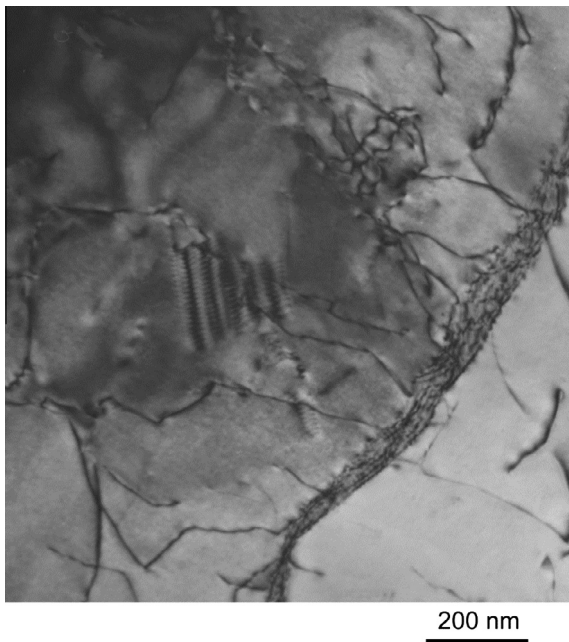
Fig. 12. A TEM micrograph showing a subgrain formed during creep at 800 °C at a stress of 75 MPa.

higher in the dislocation network than that of the bulk. Due to the cross-sectional area of the dislocation pipes, distance between the pipes, and differences in diffusion coefficients between the network and bulk, the addition proportionality was acquired [27]. Now if the sub-grain bowing is added as the internal stress, the creep exponent for power-law creep can be found to be 5 [32]. TEM was performed to identify the presence of subgrains in the specimen crept at 800 °C, shown in Fig. 12. In this figure, dislocations have formed a sub-grain boundary. From the previous analysis, it can be stated that the addition of dislocation networks and sub-grains are possible reasons for the difference between the creep mechanisms in the two elevated temperature experiments.

5. Conclusions

The creep behavior of Haynes 230 was investigated in this study at two elevated temperatures. The main findings can be summarized as follows:

1. At the stresses employed, at 900 °C the material spent a majority of its life in the tertiary creep regime, while the 800 °C results had periods of prolonged secondary creep. Intergranular failure was observed in all samples.
2. The stress exponent was found to be $n \approx 3$ at 900 °C, indicating solute drag as the creep mechanism, and $n \approx 5$ at 800 °C, indicating dislocation climb as the main creep mechanism.

3. Using high resolution digital image correlation overlaid on the microstructure, strain concentrations were found at triple junctions and grain boundary serrations.
4. The grain boundary serrations restrict grain boundary sliding and may be an effective tool to prolong the life of Haynes 230 in creeping conditions.

Acknowledgements

References

[1] INL, Next generation nuclear plant materials research and development program plan, INL/EXT-06-11701, 2006.
[2] C.H.M. Jenkins, E.H. Bucknall, E.A. Jenkinson, J. Inst. Metal. 70 (1944).
[3] M.E. Whitaker, E. Voce, A.R. Bailey, Metallurgia 39 (1948).
[4] J.N. Greenwood, J. Iron Steel Inst. 171 (1952).
[5] J.N. Greenwood, D.R. Miller, J.W. Suiter, Acta Metall. 2 (1954) 250.
[6] M.F. Ashby, C. Gandhi, D.M.R. Taplin, Acta Metall. 27 (1979) 699.
[7] A.S. Argon, Mechanics and mechanisms of fracture in creeping alloys, in: B.W.a.D.R.J Owen (Ed.), Recent Advances in Creep and Fracture of Engineering Materials and Structures, Pineridge Press, Swansea, 1982, p. 1.
[8] A.S. Argon, I.W. Chen, C.W. Lau, Intergranular cavitation in creep: theory and experiments, Creep-Fatigue-Environment Interations, Milwaukee, WI, 1979, pp. 46–83.
[9] C.W. Lau, A.S. Argon, Stress concentration caused by grain boundary sliding in metals undergoing power-law creep, in: D.M.R. Taplin (Ed.), Proc. Int. Fracture Conference, University of Waterloo Press, Waterloo, Canada, 1977, pp. 595.
[10] C.W. Lau, A.S. Argon, F.A. McClintock, Comput. Struct. 17 (1983) 923–931.
[11] L. Jiang, R. Hu, H. Kou, J. Li, G. Bai, H. Fu, Mater. Sci. Eng. A 536 (2012) 37.
[12] D. Kim, C. Jang, W. Ryu, Oxid. Met. 71 (2009) 271.
[13] M. Kun, L. Gianfranco, T. Hsiao-Ming, C. Xiang, F.S. James, J. Eng. Gas Turbines Power 133 (2011) 052908.
[14] P.K. Liaw, T.R. Leax, R.S. Williams, M.G. Peck, Acta Metall. 30 (1982) 2071.
[15] Y.L. Lu, P.K. Liaw, G.Y. Wang, M.L. Benson, S.A. Thompson, J.W. Blust, P.F. Browning, A.K. Bhattacharya, J.M. Aurrecoechea, D.L. Klarstrom, Mater. Sci. Eng. A 397 (2005) 122.
[16] G.J. Pataky, H. Sehitoglu, H.J. Maier, Mater. Charact. 75 (2013) 69.
[17] X. Chen, M.A. Sokolov, S. Sham, D.L. Erdman Iii, J.T. Busby, K. Mo, J.F. Stubbins, J. Nucl. Mater. 432 (2013) 94.
[18] C.J. Boehlert, S.C. Longanbach, Mater. Sci. Eng. A 528 (2011) 4888.
[19] J.M. Larson, S. Floreen, Metall. Trans. A 8 (1977) 51–55.
[20] M. Zhiping, Y. Ruizeng, G. Liang, Mater. Sci. Technol. 4 (1988) 540.
[21] M. Sutton, J.-J. Orteu, H. Schreier, Image Correlation for Shape Motion and Deformation Measurements: Basic Concepts, Theory and Applications, Spring Media, 2009.
[22] M.A. Sutton, W.J. Wolters, W.H. Peters, W.F. Ranson, S.R. McNeill, Image Vis. Comput. 1 (1983) 133.
[23] J. Carroll, W. Abuzaid, J. Lambros, H. Sehitoglu, Rev. Sci. Instrum. 81 (2010) 083703.
[24] J. Weertman, J. Appl. Phys. 26 (1955) 1213–1217.
[25] J. Weertman, J. Appl. Phys. 28 (1957) 362–364.
[26] A.H. Cottrell, M.A. Jawson, Proc. R. Soc. A 199 (1949) 104–114.
[27] F.R.N. Nabarro, H.L. de Villiers, The Physics of Creep: Creep and Creep-resistant Alloys, Taylor & Francis, London, 1995.
[28] M.E. Kassner, M.-T. Pérez-Prado, Prog. Mater Sci. 45 (2000) 1–102.
[29] H. Suzuki, J. Phys. Soc. Jpn. 17 (1962) 322–325.
[30] C.K.L. Davies, P.W. Davies, B. Wilshire, Phil. Mag. 12 (1965) 827.
[31] M.M. Myshlyaev, Annu. Rev. Mater. Sci. 11 (1981) 31–50.
[32] A.S. Argon, S. Takeuchi, Acta Metall. 29 (1981) 1877.